AIMS Mathematics, 11(11): 37024–37049.
DOI: 10.3934/math.20261431
Received: 30 July 2026
Revised: 16 October 2026
Accepted: 22 October 2026
Published: 09 November 2026

http://www.aimspress.com/journal/Math

Research article

Transition to turbulence in an infinite-Prandtl Rayleigh-Bénard problem

Darío Martínez, Henar Herrero* and Francisco Pla

Departamento de Matemáticas, IMACI, Facultad de Ciencias y Tecnologías Quíımicas Universidad de Castilla-La Mancha, 13071 Ciudad Real, Spain

* **Correspondence:** Email: Henar.Herrero@uclm.es.

Abstract: The transition from steady convection to turbulent dynamics in the two-dimensional Rayleigh–Bénard problem with an infinite Prandtl number was investigated by means of high-resolution numerical simulations. The computations were performed using an implicit overlapping Schwarz domain decomposition method combined with Legendre collocation discretizations, allowing accurate resolution of both stationary and strongly unsteady flow regimes. The numerical results revealed the existence of a subcritical transition near $Ra \approx 2.5 \times 10^5$, where the classical steady three-roll solution loses stability and gives rise to an intermittent regime. The post-critical dynamics are characterized by the coexistence of two competing flow states: a quasi-laminar four-roll configuration and a plume-dominated three-roll configuration exhibiting small-scale vortical structures and enhanced fluctuation levels. This coexistence generates complex dynamics involving intermittency, multi-stability, and hysteresis over a broad range of Rayleigh numbers. The transition was analyzed through flow visualizations, fluctuation diagnostics, and statistical characterization of the temperature field. Space–time representations and point-wise fluctuation signals revealed alternating episodes associated with the two flow organizations. Statistical analyses showed that Gaussian behavior is recovered only over restricted temporal intervals, whereas longer datasets exhibit non-Gaussian features that are accurately described by Gaussian-mixture models, providing quantitative evidence of the coexistence of multiple dynamical states. The influence of the transition on heat transport was quantified through the Nusselt number. The bifurcation diagrams obtained by forward and backward continuation revealed several hysteresis loops and distinct heat-transfer branches. Interestingly, the quasi-laminar four-roll state systematically produces larger Nusselt numbers than the turbulent state, indicating a more efficient heat-transfer mechanism despite its lower level of flow complexity. Power-law regressions for both branches yielded scaling exponents close to the classical $Nu \sim Ra^{1/3}$ law. The computed transition thresholds, the hysteresis structure, flow patterns, and scaling laws are in good agreement with previous numerical and experimental studies, supporting both the reliability of the proposed methodology and the physical interpretation of the observed intermittent dynamics.

Keywords: Rayleigh–Bénard convection; turbulence; Legendre collocation; domain decomposition

method

Mathematics Subject Classification: 35Q35, 65N35, 76E06

1. Introduction

Rayleigh–Bénard convection is one of the fundamental paradigms in fluid dynamics, nonlinear science, and pattern formation. It describes the motion of a fluid layer heated from below and cooled from above, where buoyancy forces compete with viscous and thermal diffusion effects. Due to its simple formulation and rich dynamical behavior, Rayleigh–Bénard convection has become a canonical framework for investigating hydrodynamic instabilities, bifurcation phenomena, pattern selection, transition to turbulence, and heat transport mechanisms [1, 3, 31]. Beyond its theoretical importance, it plays a key role in numerous applications, including atmospheric circulation, oceanic dynamics, crystal growth processes, industrial heat transfer, and geophysical flows [4, 39, 48].

Particularly relevant is the limit of large or infinite Prandtl numbers. In this regime, inertial effects become negligible and the flow dynamics are governed by the interplay between buoyancy and viscous forces. This limit provides an accurate approximation for highly viscous fluids and for several geophysical convection processes. In particular, mantle convection models are commonly formulated in the infinite-Prandtl-number limit due to the extremely large effective viscosity of mantle rocks [19, 38, 51]. As a consequence, understanding of flow transitions, heat transport, coherent structures, and turbulent dynamics in high-Prandtl-number Rayleigh–Bénard systems is of considerable importance for the mathematical modeling of Earth's mantle dynamics and thermal evolution [27, 51, 55].

The dynamics of Rayleigh–Bénard convection are mainly controlled by two dimensionless parameters: the Rayleigh number Ra and the Prandtl number Pr. The Rayleigh number measures the relative strength of buoyancy forcing with respect to dissipative effects, whereas the Prandtl number represents the ratio of kinematic viscosity to thermal diffusivity. As the Rayleigh number increases, the conductive state loses stability, and a sequence of bifurcations may lead to increasingly complex dynamical regimes. One of the central challenges in fluid mechanics is characterizing the mechanisms governing the transition from coherent convective structures to turbulent flows and determining how these transitions affect heat transport.

Although turbulence is inherently three-dimensional, previous studies have shown that two-dimensional and three-dimensional Rayleigh–Bénard convection exhibit remarkable similarities in the infinite-Prandtl-number limit [7, 43, 45, 50]. In this regime, the flow tends to become quasi-two-dimensional due to the strong suppression of horizontal velocity components, making two-dimensional simulations a valuable tool for investigating turbulent convection and associated heat-transfer processes.

A large variety of numerical methodologies have been developed for the direct numerical simulation of Rayleigh–Bénard convection. Comparative assessments of available computational approaches can be found in [28]. Finite-difference discretizations have been employed in [20, 56, 49], finite-volume formulations in [52, 58], spectral-element methods in [18, 43], and spectral approaches in [29]. Among high-order methods, spectral collocation techniques are particularly attractive because of their

accuracy in resolving complex flow structures and sharp thermal gradients. In the present work, the computations are performed using an implicit Schwarz domain decomposition method combined with Legendre collocation discretizations and second-order finite-difference-time integration [35, 36, 37]. Previous studies demonstrated the efficiency and convergence properties of this methodology for stationary and time-dependent convection problems. Here, the method is used to perform high-resolution simulations of strongly nonlinear and turbulent convection regimes, providing a stringent assessment of its capabilities in complex dynamical scenarios.

Most available studies on high- or infinite-Prandtl-number convection focus on global heat-transfer properties and scaling laws relating the Nusselt and Rayleigh numbers. Classical theoretical, numerical, and experimental investigations suggest power laws of the form $Nu \sim Ra^{1/3}$ [2, 15, 20], often with different prefactors [6, 40, 53]. Alternative exponents, including $2/7$ and $5/19$, have also been proposed [1, 60], together with logarithmic corrections in asymptotic regimes [42]. Although these studies have significantly improved the understanding of turbulent heat transport, comparatively less attention has been devoted to the dynamical mechanisms responsible for the transition between coherent convective states and turbulent flow in the infinite-Prandtl-number limit.

The transition to turbulence in Rayleigh–Bénard convection has been investigated experimentally, theoretically, and numerically. Observed scenarios include sequences of secondary bifurcations, oscillatory instabilities, boundary-layer instabilities, large-scale circulation reversals, plume intermittency, and turbulent roll dynamics [1, 12, 17, 29]. Intermittent behavior has been reported in both experiments and simulations, and has been associated with the coexistence of competing dynamical states [13, 14, 34]. Similar phenomena have recently been identified in infinite-Prandtl-number convection, where turbulent plume dynamics coexist with persistent coherent structures [57, 61].

The main objective of the present work is to provide a detailed mathematical and computational characterization of the transition to turbulence in two-dimensional Rayleigh–Bénard convection with an infinite Prandtl number. Particular emphasis is placed on the identification of flow regimes, the analysis of intermittency, the characterization of fluctuation statistics, and the impact of the transition on heat transport. Unlike previous investigations focused primarily on global scaling laws, the present study combines high-resolution spectral simulations, bifurcation analysis, statistical diagnostics, and heat-transfer measurements to reveal the existence of a subcritical transition leading to the coexistence of two competing flow states: a quasi-laminar four-roll configuration and a plume-dominated three-roll configuration. The resulting dynamics exhibit intermittency, multistability, and hysteresis over a broad range of Rayleigh numbers. In addition, Gaussian-mixture models are employed to characterize the fluctuation statistics, providing quantitative evidence for the coexistence of multiple dynamical states.

The remainder of the paper is organized as follows. Section 2 presents the mathematical formulation. Section 3 offers the numerical methodology. Section 4 describes the computational setup and validation procedures. Section 5 is devoted to the numerical results and the analysis of the transition dynamics. Finally, Section 6 summarizes the main conclusions.

2. Formulation of the problem

Mantle convection is modeled as buoyancy-driven thermal convection in a highly viscous incompressible fluid layer heated from below and cooled from above [16]. The physical domain is

idealized as a two-dimensional rectangular cavity of length L and depth d, whose lower and upper boundaries are maintained at constant temperatures T_1 and T_0, respectively, with $T_1 > T_0$. Let $\mathbf{u}$ denote the velocity field, p the pressure, and θ the temperature. Under the Boussinesq approximation, the fluid is characterized by a reference density ρ_0, dynamic viscosity μ, thermal diffusivity κ, thermal expansion coefficient α, and gravitational acceleration g acting in the direction of the unit vector $\mathbf{e}_z$ [8]. The kinematic viscosity is defined as $\nu = \mu/\rho_0$. A distinctive feature of mantle convection is the extremely large value of the Prandtl number:

$$Pr = \frac{\nu}{\kappa} \gg 1.$$

In the asymptotic regime $Pr \to \infty$, which is appropriate for the mantle of the Earth [26, 44], inertial effects become negligible compared to viscous forces. As a consequence, the momentum equation reduces to a Stokes balance between viscous stresses, pressure gradients, and thermal buoyancy. Using d as the characteristic length scale, $\Delta T = T_1 - T_0$ as the temperature scale, κ/d as the velocity scale, $\rho_0 \kappa \nu / d^2$ as the pressure scale, and d^2/κ as the time scale, the governing equations take the non-dimensional form

$$\begin{aligned} \nabla \cdot \mathbf{u} &= 0, && (2.1)\\ -\Delta \mathbf{u} + \nabla p - Ra\, \theta\, \mathbf{e}_z &= 0, && (2.2)\\ \partial_t \theta - \Delta \theta + \mathbf{u} \cdot \nabla \theta &= 0, && (2.3) \end{aligned}$$

where the Rayleigh number is defined by

$$Ra = \frac{\alpha g\, d^3\, \Delta T}{\nu \kappa}.$$

The Rayleigh number is the principal control parameter of the system, measuring the relative importance of thermal buoyancy with respect to viscous and diffusive effects and governing the transition from conductive to convective heat transport. The dimensionless problem is posed in the space-time domain $\Omega \times (0, \mathcal{T}]$, where $\mathcal{T} > 0$ denotes the final integration time and

$$\Omega = (0, \Gamma) \times (0, 1), \qquad \Gamma = \frac{L}{d}.$$

The initial conditions are given by

$$\mathbf{u}(x, z, 0) = \mathbf{u}_0(x, z), \qquad \theta(x, z, 0) = \theta_0(x, z), \qquad p(x, z, 0) = p_0(x, z), \quad (x, z) \in \Omega, \tag{2.4}$$

where $\mathbf{u}_0$, θ_0, and p_0 satisfy the prescribed boundary conditions. Following standard mantle convection models [38], no-slip conditions are imposed at the lower boundary, whereas free-slip conditions are considered at the upper and lateral boundaries. The temperature is fixed on the horizontal boundaries, while the vertical walls are assumed to be thermally insulated:

$$\begin{aligned} &\mathbf{u} = \mathbf{0}, \qquad \theta = 1, \qquad z = 0, && (2.5)\\ &\partial_z u_x = 0, \quad u_z = 0, \quad \theta = 0, \qquad z = 1, && (2.6)\\ &u_x = 0, \quad \partial_x u_z = 0, \quad \partial_x \theta = 0, \qquad x = 0, \Gamma. && (2.7) \end{aligned}$$

The pressure boundary conditions are obtained from the normal component of the momentum equations on $x = 0$, $x = \Gamma$, and $z = 1$, together with the incompressibility constraint on $z = 0$ (see [21, 22]). For the numerical formulation, it is convenient to homogenize the thermal boundary conditions by introducing the transformed variable

$$\hat{\theta} = \theta - (1 - z).$$

In terms of $\hat{\theta}$, all temperature boundary conditions become homogeneous. Omitting the hat notation for simplicity, the boundary conditions can be written compactly as

$$\mathcal{B}(\mathbf{u}, \theta, p) = 0,$$

where

$$\mathcal{B}(\mathbf{u}, \theta, p) = \Big(\mathbf{u}|_{z=0},\ \theta|_{z=0} - 1,\ (\partial_z u_x, u_z, \theta)|_{z=1},\ (u_x, \partial_x u_z, \partial_x \theta)|_{x=0,\Gamma},\ \mathcal{B}_p(\mathbf{u}, \theta, p)\Big),$$

and $\mathcal{B}_p$ denotes the pressure boundary operator,

$$\mathcal{B}_p(\mathbf{u}, \theta, p) = \Big((-\Delta u_x + \partial_x p)|_{x=0,\Gamma}, (-\Delta u_z + \partial_z p - Ra\theta)|_{z=1}, (\nabla \cdot u)|_{z=0}\ \Big).$$

3. Numerical method

The temporal discretization is performed by means of the second-order semi-implicit scheme proposed in [54]. Given $(\mathbf{u}^k, p^k, \theta^k)$ and $(\mathbf{u}^{k-1}, p^{k-1}, \theta^{k-1})$, the approximation $(\mathbf{u}^{k+1}, p^{k+1}, \theta^{k+1})$ is defined as the solution of

$$-\Delta \mathbf{u}^{k+1} + \nabla p^{k+1} = Ra\,\theta^k \mathbf{e}_z, \qquad \text{in } \Omega, \tag{3.1}$$

$$\nabla \cdot \mathbf{u}^{k+1} = 0, \qquad \text{in } \Omega, \tag{3.2}$$

$$\frac{3\theta^{k+1} - 4\theta^k + \theta^{k-1}}{2h} + \mathbf{u}^k \cdot \nabla \theta^{k+1} - \Delta \theta^{k+1} = 0, \qquad \text{in } \Omega, \tag{3.3}$$

$$\mathcal{B}\left(\mathbf{u}^{k+1}, \theta^{k+1}, p^{k+1}\right) = 0, \qquad \text{on } \partial\Omega, \tag{3.4}$$

where $h = \Delta t$ denotes the time step and

$$(\mathbf{u}^k, p^k, \theta^k) = (\mathbf{u}(x, z, t_k), p(x, z, t_k), \theta(x, z, t_k)), \qquad t_k = kh, \qquad k = 0, 1, 2, \ldots.$$

The sequence is initialized from the prescribed initial conditions. For each time level, system (3.1)–(3.4) defines a coupled elliptic problem for the unknowns $(\mathbf{u}^{k+1}, p^{k+1}, \theta^{k+1})$. To solve this problem, an overlapping Schwarz domain decomposition method is employed [23, 35, 36, 37]. The computational domain $\Omega = (0, \Gamma) \times (0, 1)$ is decomposed into a family of overlapping subdomains

$$\Omega = \bigcup_{i=1}^{n} \bigcup_{j=1}^{m} \Omega_{ij},$$

where

$$\Omega_{ij} = \left(\frac{i-1}{n}(\Gamma - \gamma), \frac{i\Gamma + (n-i)\gamma}{n}\right) \times \left(\frac{j-1}{m}(1 - \gamma), \frac{j + (m-j)\gamma}{m}\right), \qquad \begin{matrix} i = 1, \ldots, n \\ j = 1, \ldots, m \end{matrix},$$

where γ denotes the overlap width. The partition parameters are selected such that all subdomains have identical dimensions and overlap widths. Denoting the restriction of the solution to Ω_{ij} by

$$(\mathbf{u}_{ij}, p_{ij}, \theta_{ij}) = (\mathbf{u}, p, \theta)|_{\Omega_{ij}},$$

the Schwarz formulation consists of solving the following problem in each subdomain:

$$-\Delta \mathbf{u}_{ij}^{k+1} + \nabla p_{ij}^{k+1} = Ra\, \theta_{ij}^{k} \mathbf{e}_z, \qquad \text{in } \Omega_{ij}, \tag{3.5}$$

$$\nabla \cdot \mathbf{u}_{ij}^{k+1} = 0, \qquad \text{in } \Omega_{ij}, \tag{3.6}$$

$$\frac{3\theta_{ij}^{k+1} - 4\theta_{ij}^{k} + \theta_{ij}^{k-1}}{2h} + \mathbf{u}_{ij}^{k} \cdot \nabla \theta_{ij}^{k+1} - \Delta \theta_{ij}^{k+1} = 0, \qquad \text{in } \Omega_{ij}, \tag{3.7}$$

together with the original boundary conditions on $\partial\Omega_{ij} \cap \partial\Omega$ and the transmission conditions

$$\left(\mathbf{u}_{ij}, \theta_{ij}, p_{ij}\right) = \left(\mathbf{u}_{i'j'}, \theta_{i'j'}, p_{i'j'}\right) \qquad \text{on } \partial\Omega_{ij} \cap \Omega_{i'j'}, \tag{3.8}$$

for every neighboring subdomain $\Omega_{i'j'}$. The convergence of the Schwarz operator follows from the overlap of adjacent subdomains, as proven in [23, 36, 37]. The solution of every subdomain problem (3.5)–(3.8) is calculated using a Legendre collocation method. To this end, each subdomain is mapped onto the reference square $\widehat{\Omega} = (-1, 1)^2$ through an affine transformation. The approximating space is then defined as

$$\mathbb{P}_{N-1} \otimes \mathbb{P}_{M-1},$$

and the numerical solution is sought in the form

$$f_{NM}(x, z) = \sum_{p=0}^{N-1} \sum_{q=0}^{M-1} \widehat{f_{pq}} L_p(x) L_q(z), \tag{3.9}$$

where L_p denotes the Legendre polynomial of degree p. The collocation equations are obtained by enforcing the differential system and the transmission conditions at the Legendre–Gauss–Lobatto nodes. This procedure leads to a linear system for the coefficients $\widehat{f_{pq}}$, which is solved using MATLAB's built-in Gaussian elimination routines, yielding the numerical solution [5, 9].

The resulting discretization may be interpreted as a high-order domain-decomposition collocation scheme. For computational convenience, the width of the overlap is fixed so that the collocation points of adjacent subdomains coincide. Thus, the overlap is characterized by the number of collocation points in each overlap region, denoted by *ov*.

4. Computational setup and validation

The purpose of this study is to investigate the sequence of flow regimes that arise in Rayleigh–Bénard convection as the Rayleigh number increases. To this end, a continuation procedure is used with respect to Ra starting from $Ra = 1.1 \times 10^3$ and progressing to $Ra = 5.5 \times 10^5$. At each continuation step, the final numerical solution computed at the previous Rayleigh number is used as the initial condition. The computational parameters, the quantities used to characterize the solutions, and the validation of the numerical methodology are presented in this section.

4.1. Numerical setup

In numerical simulations, the aspect ratio is fixed at $\Gamma = 3.495$, as determined in previous analyses [24, 44]. Time integration is performed with a constant time step $h = 10^{-4}$. A Legendre–Gauss–Lobatto collocation discretization with 14×14 nodes is used within each subdomain, yielding local polynomial approximations of degree 13 in both spatial directions. The computational domain is partitioned into a 13×3 array of overlapping Schwarz subdomains. Following the analysis reported in [35], the value $ov = 4$ was chosen as the best trade-off between accuracy and computational efficiency. For stationary regimes, computations are carried out until convergence is achieved, which typically requires approximately 10^3 time steps. For unsteady solutions, integration intervals of 2.5×10^5 time steps are used for $Ra \geq 2.5 \times 10^5$. Thus, statistically convergent estimates of the relevant time-averaged quantities are ensured.

4.2. Quantities of interest

The analysis is based on the temperature and velocity fields together with two derived quantities: the temperature fluctuations and the Nusselt number. The temperature fluctuation is defined as

$$\Theta(x, z, t) = \theta(x, z, t) - \langle \theta(x, z, t) \rangle_t, \tag{4.1}$$

where $\langle \cdot \rangle_t$ denotes the temporal averaging

$$\langle \theta(x, z, t) \rangle_t = \frac{1}{\mathcal{T}} \int_0^{\mathcal{T}} \theta(x, z, t)\, dt. \tag{4.2}$$

The global heat-transfer rate is characterized by the Nusselt number

$$Nu(Ra, t) = \frac{1}{\Gamma} \int_0^{\Gamma} \int_0^1 (\theta u_z - \partial_z \theta)\, dz\, dx, \tag{4.3}$$

and its time average,

$$Nu(Ra) = \left\langle \frac{1}{\Gamma} \int_0^{\Gamma} \int_0^1 (\theta\, u_z - \partial_z \theta) dz dx \right\rangle_t = \frac{1}{\mathcal{T}} \frac{1}{\Gamma} \int_0^{\mathcal{T}} \int_0^{\Gamma} \int_0^1 (\theta\, u_z - \partial_z \theta) dz dx dt. \tag{4.4}$$

The dependence of Nu on Ra is a standard indicator for identifying changes in the heat-transfer mechanisms and flow dynamics in Rayleigh–Bénard convection [1, 6, 30, 40, 41].

4.3. Convergence and validation

Spatial convergence studies of the numerical algorithms used in this work have previously been reported for stationary solutions in [36, 37]. For unsteady solutions, and particularly for turbulent regimes, the validation strategy is based on the convergence of statistically averaged quantities. The Nusselt number is commonly used for this purpose [46, 47].

The values reported in Table 1 correspond to $Ra = 2.5 \times 10^5$. The mesh-convergence results are obtained by maintaining a fixed local discretization of the $N \times M = 14 \times 14$ collocation points per subdomain and progressively refining the global mesh through an increase in the number of subdomains, from $n \times m = 13 \times 3$, 16×4, 19×5, 22×6, 25×7, and 28×8. This leads to a

total of 7644, 12544, 18620, 25872, 34300, and 43904 mesh points, respectively. The mean Nusselt number obtained over all the meshes considered is

$$Nu = 7.26 \pm 0.07,$$

i.e., the standard deviation remains below 1% of the corresponding mean value. Moreover, this value is consistent with the experimental correlation reported in [59], $Nu = 0.243\, Ra^{0.274} = 7.32$. A complementary assessment of spatial convergence is provided in Figure 1, which displays the temporal evolution of the Nusselt number, $Nu(t)$, for the discretizations considered. The curves are similar, indicating that the essential dynamical and heat-transfer features of the flow are accurately captured even on the coarser meshes. Based on these results, a decomposition consisting of 13×3 overlapping subdomains, each discretized by a 14×14 Legendre–Gauss–Lobatto collocation mesh, was selected for all subsequent simulations. This configuration corresponds to a total of 7644 collocation points and offers an excellent compromise between numerical accuracy and computational efficiency.

Table 1. Nusselt number and computational times against the number of mesh points for $Ra = 2.5 \times 10^5$.

	7644	12544	18620	25872	34300	43904
Nu	7.25	7.33	7.15	7.31	7.31	7.24
time [h]	0.5	1.3	2.9	4.6	8.4	13.9

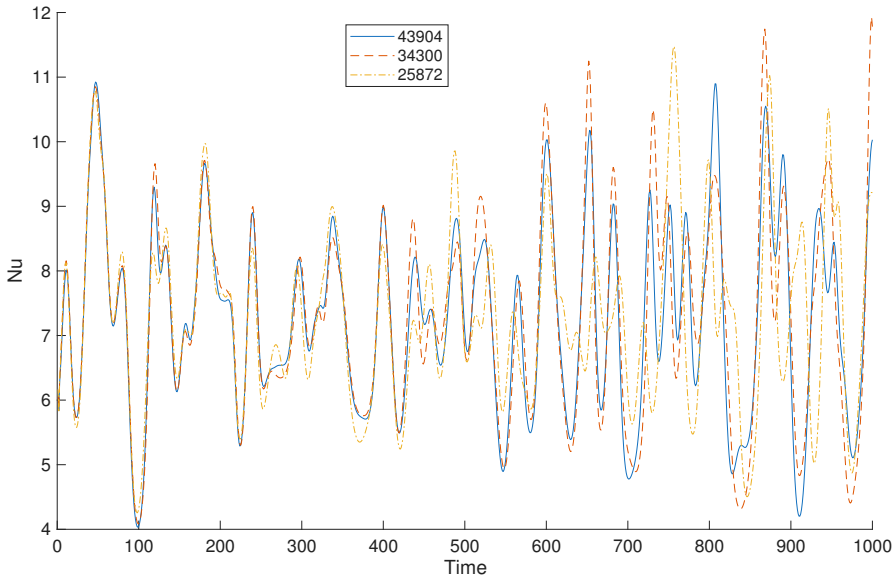


Figure 1. $Nu(t)$ defined by Eq (4.3), for $Ra = 2.5 \times 10^5$, at different numbers of mesh points.

The Nusselt number $Nu(Ra)$ was then evaluated for all Rayleigh numbers considered in this study. To assess the statistical convergence of the simulations, the running temporal average defining Nu was monitored throughout the integrations. Figure 2a) and 2b) show this quantity as a function of the final integration time for $Ra = 2.5 \times 10^5$ and $Ra = 4.0 \times 10^5$, respectively. In both cases, the running

average approaches a stable asymptotic value, indicating convergence of the statistical estimator used to compute the Nusselt number. These results confirm that the integration times employed are sufficiently long to obtain statistically converged heat-transfer rates.

Additionally, the computational times corresponding to the different spatial discretizations are reported in Table 1. As expected, the execution time increases significantly with the spatial resolution when computations are performed in a sequential environment. Nevertheless, the Schwarz–Legendre methodology has excellent parallelization properties [36], making it particularly suitable for large-scale computations and substantially reducing computational cost in parallel implementations.

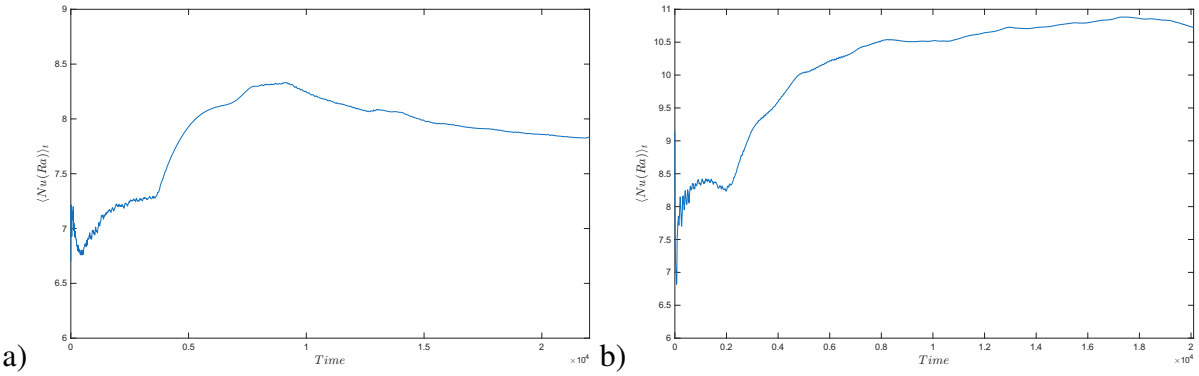


Figure 2. Mean value of the Nusselt number depending on time. a) $Ra = 2.5 \times 10^5$, b) $Ra = 4.0 \times 10^5$.

5. Numerical results

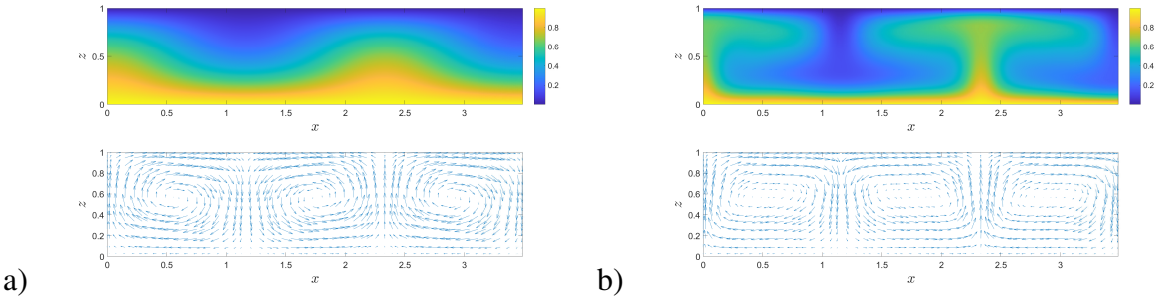
The numerical simulations reveal a sequence of dynamical transitions as the Rayleigh number increases. The most significant result is the appearance of an intermittent regime in which two competing flow configurations coexist: a quasi-laminar four-roll state and a plume-dominated three-roll state. The existence of this regime is investigated through flow visualizations, fluctuation analysis, statistical characterization, and heat-transfer measurements.

5.1. Flow patterns and regime transitions

Following the primary bifurcation of the conductive state at $Ra_c = 1100$ [44], a steady three-roll convective solution emerges. This flow structure remains stable over the interval

$$1100 \leq Ra < 2.5 \times 10^5,$$

while undergoing substantial quantitative changes. In particular, the thermal field evolves from smooth nearly sinusoidal profiles to increasingly localized mushroom-shaped structures as nonlinear effects become more pronounced. Representative solutions of this regime are shown in Figure 3 for $Ra = 1300$ and $Ra = 2.49 \times 10^5$.



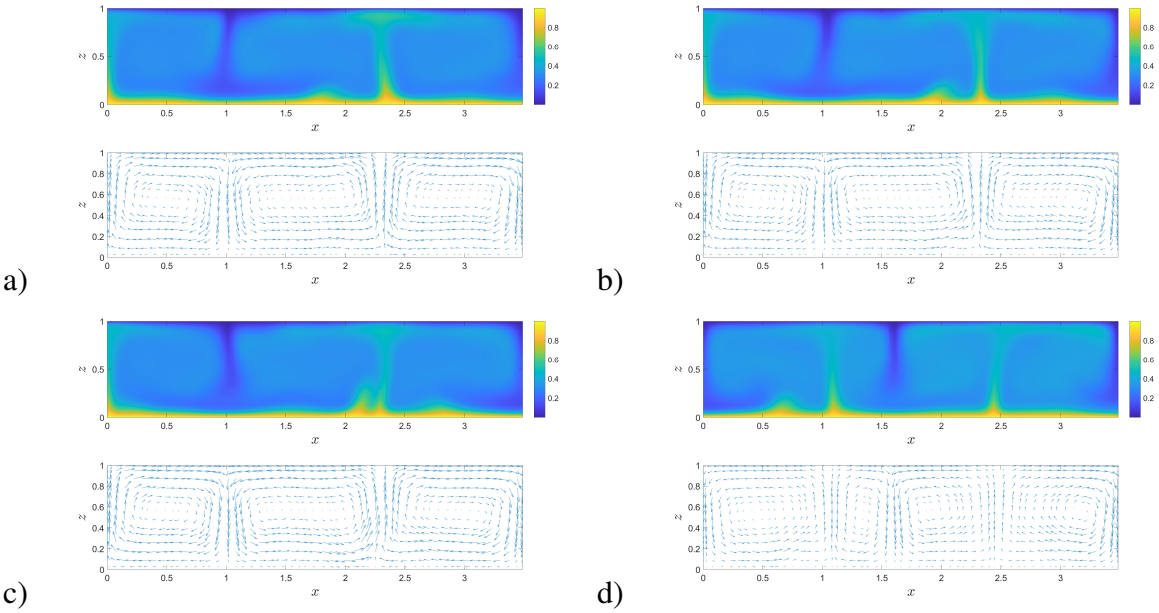
a) b)

Figure 3. Color maps of the numerical temperature (top) and numerical velocity fields (bottom) at a) $Ra = 1300$; b) $Ra = 2.49 \times 10^5$.

A qualitative transition occurs at approximately

$$Ra = 2.5 \times 10^5,$$

where the steady solution loses stability. Beyond this value, the flow no longer converges to a stationary state and instead alternates between two different dynamical configurations. The first consists of a coherent four-roll circulation with relatively weak fluctuations. The second is characterized by intense plume emission, eddy formation, and roll interactions within an overall three-roll circulation. Representative snapshots of the transition are presented in Figures 4 and 5.



a) b)

c) d)

Figure 4. Color maps of the numerical temperature (top) and numerical velocity fields (bottom) at $Ra = 2.5 \times 10^5$ and successive times. The process depicted is the generation of eddies and plumes at the bottom.

The alternation between these two states persists throughout the interval

$$2.5 \times 10^5 \leq Ra \leq 5.5 \times 10^5,$$

indicating that turbulence develops through an intermittent mechanism rather than through the complete destruction of the large-scale circulation. Similar intermittent behavior has previously been reported in numerical and experimental studies of Rayleigh–Bénard convection [1, 57, 62, 63]. The turbulent states are characterized by strong thermal plume activity originating in the boundary layers and by the generation of small-scale vortical structures, in agreement with the observations reported in [29, 33, 61].

Overall, the simulations suggest the coexistence of two competing attractors over a broad range of Rayleigh numbers, motivating a more detailed quantitative analysis of the fluctuation dynamics and heat-transfer properties.

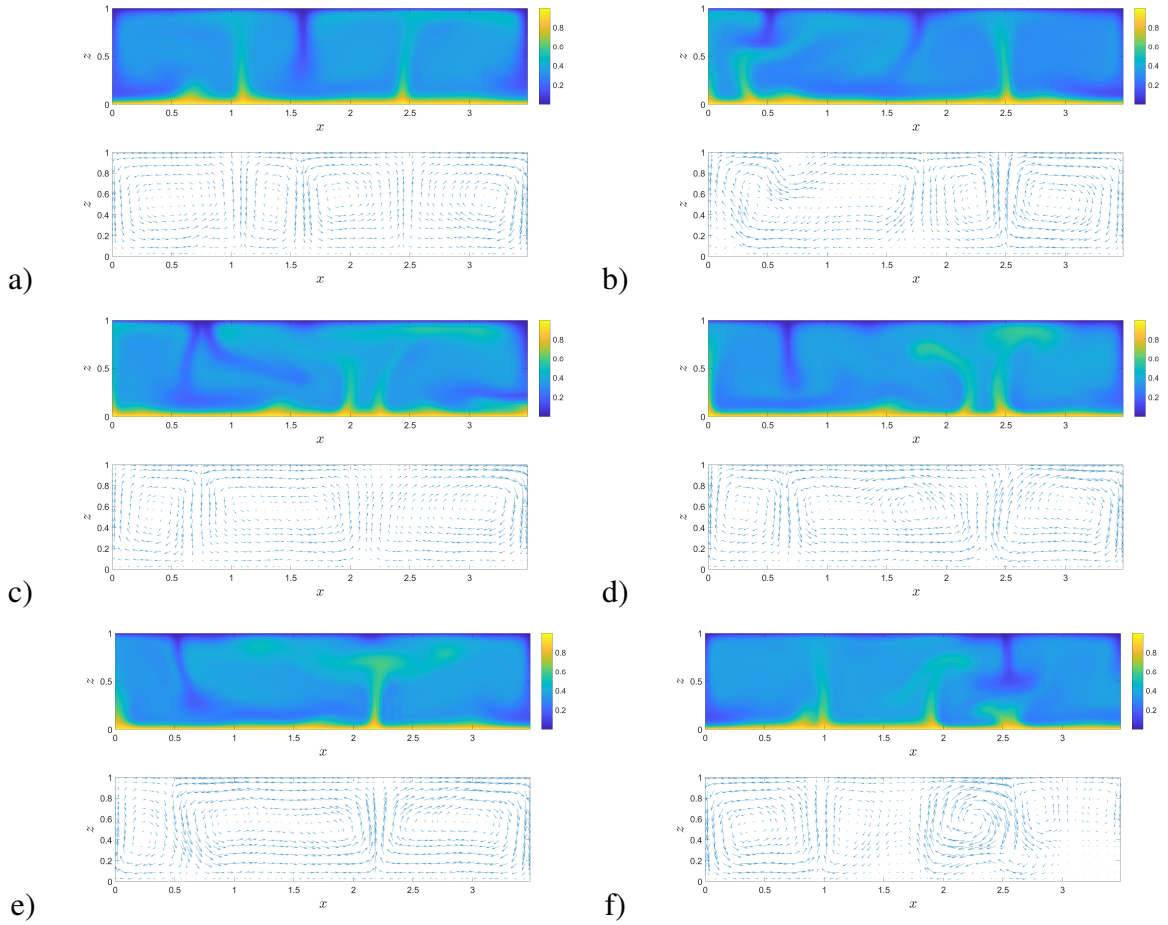


Figure 5. Color maps of the numerical temperature (top) and numerical velocity field (bottom) at $t = 5 \times 10^5$ for a) $Ra = 3.0 \times 10^5$; b) $Ra = 3.5 \times 10^5$; c) $Ra = 4.0 \times 10^5$; d) $Ra = 4.5 \times 10^5$; e) $Ra = 5 \times 10^5$; f) $Ra = 5.5 \times 10^5$.

5.2. Fluctuation analysis

Beyond the qualitative information provided by the flow visualizations, turbulent intermittency can be further quantified through the analysis of fluctuations of the relevant physical variables. Since all flow fields exhibit essentially the same qualitative behavior, only temperature fluctuations are considered here for the sake of brevity.

These fluctuations are defined as the deviation of the instantaneous temperature from its temporal mean at a given spatial location and are given by Eq (4.1). Figure 6 shows space–time contour plots of the temperature fluctuation field for $Ra = 2.5 \times 10^5$, evaluated along horizontal sections of the domain at the fixed heights $z = 0.0259$ (Figure 6a)) and $z = 0.9741$ (Figure 6b)). The two flow states identified previously are clearly visible. A quasi-laminar regime, associated with a coherent four-roll circulation pattern, occupies the time intervals $2.5\times10^3 h \le t \le 7.5\times10^3 h$ and $1.2\times10^4 h \le t \le 1.4\times10^4 h$. Outside these intervals, the flow exhibits a more turbulent state characterized by roll interactions, roll collisions, thermal plume emission, and the development of small-scale vortical structures. During these turbulent phases, the large-scale circulation is predominantly organized into a three-roll configuration.

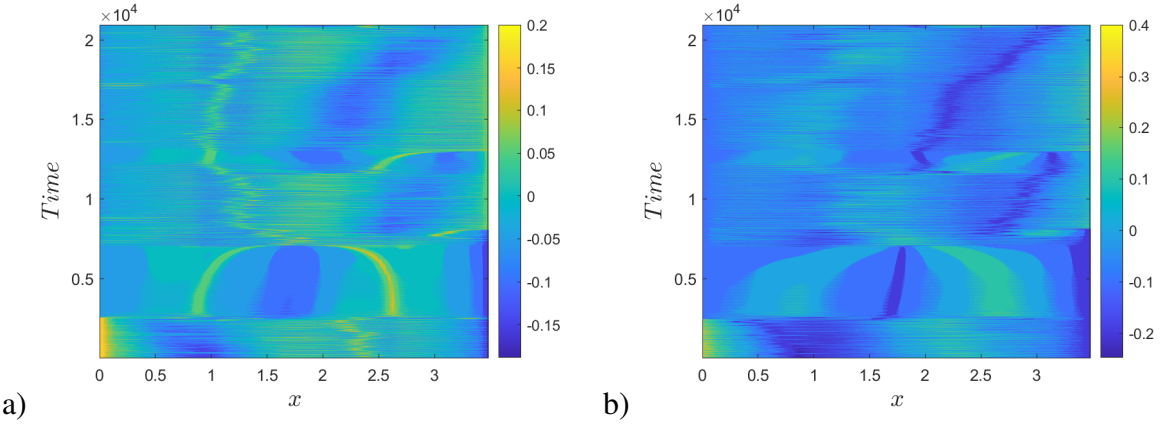
The corresponding fluctuation fields for $Ra = 4 \times 10^5$ are shown in Figure 7. As before, the fluctuations are shown at $z = 0.0259$ (Figure 7a)) and $z = 0.9741$ (Figure 7b)). The flow alternates between two distinct states. A turbulent regime, characterized by intense plume activity and small-scale vortices embedded within a three-roll large-scale circulation, is observed for $0 \le t \le 0.2 \times 10^4$ and $1.8 \times 10^4 \le t \le 2 \times 10^4$. The remaining portion of the simulation is dominated by a quasi-laminar four-roll structure. The recurrent alternation between these two states provides further evidence of the intermittent character of the flow dynamics at this Rayleigh number.

To further investigate the intermittent dynamics, temperature fluctuations were monitored at several representative locations within the domain. Figure 8 shows the fluctuation time series for $Ra = 2.5\times10^5$ at locations $(x, z) = (1.334, 0.9741)$, $(1.7278, 0.4772)$, and $(1.052, 0.0259)$, respectively. Similarly, Figure 9 presents the fluctuation time series for $Ra = 4.0 \times 10^5$ at locations $(x, z) = (2.7413, 0.9741)$, $(2.3668, 0.4772)$, and $(2.8996, 0.0259)$, respectively. For $Ra = 2.5 \times 10^5$, the intermittent nature of the flow is readily identified in the fluctuation signals. The quasi-laminar intervals previously detected in Figure 6, namely, $0.25 \times 10^4 h \le t \le 0.75 \times 10^4 h$ and $1.2 \times 10^4 h \le t \le 1.4 \times 10^4 h$, are characterized by relatively small fluctuation amplitudes, consistent with the persistence of an organized four-roll circulation. Outside these intervals, the signals become increasingly irregular and exhibit larger excursions, reflecting the onset of the turbulent state and the associated enhancement of plume activity and flow complexity.

A comparison within Figure 8 also reveals a pronounced spatial dependence of the fluctuations. Significantly larger amplitudes are observed near the upper and lower boundaries than at the interior monitoring point, indicating that turbulent activity is concentrated primarily within the near-wall regions. In contrast, the core of the domain exhibits weaker fluctuations and more coherent dynamical behavior, suggesting greater persistence of the large-scale circulation.

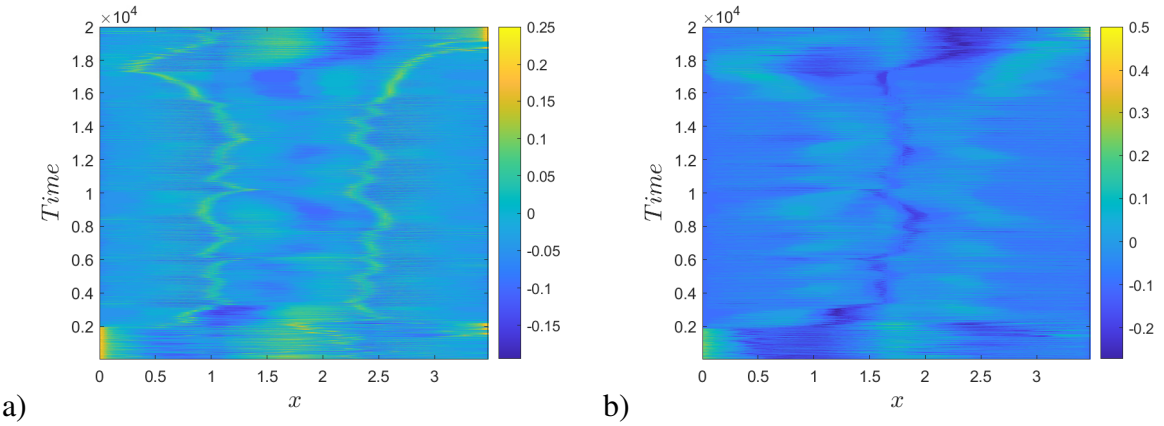
A similar spatial distribution is observed for $Ra = 4.0\times10^5$ (Figure 9), where the largest fluctuation amplitudes are again found close to the horizontal boundaries. However, unlike the lower-Rayleigh-number case, the time series alone do not provide a clear distinction between the quasi-laminar and turbulent states. The quasi-laminar regime itself exhibits appreciable temporal variability, reducing the contrast between the two dynamical states. Consequently, the corresponding temporal intervals cannot be identified unambiguously from single-point measurements. Nevertheless, the two regimes remain

clearly distinguishable in the space–time contour plots of Figure 7, where their different large-scale flow organizations and plume dynamics are readily apparent.



a) b)

Figure 6. Temperature fluctuations on a horizontal axis over time for $Ra = 2.5 \times 10^5$ at a) $z = 0.0259$, b) $z = 0.9741$.



a) b)

Figure 7. Temperature fluctuations on a horizontal axis over time for $Ra = 4 \times 10^5$ at a) $z = 0.0259$, b) $z = 0.9741$.

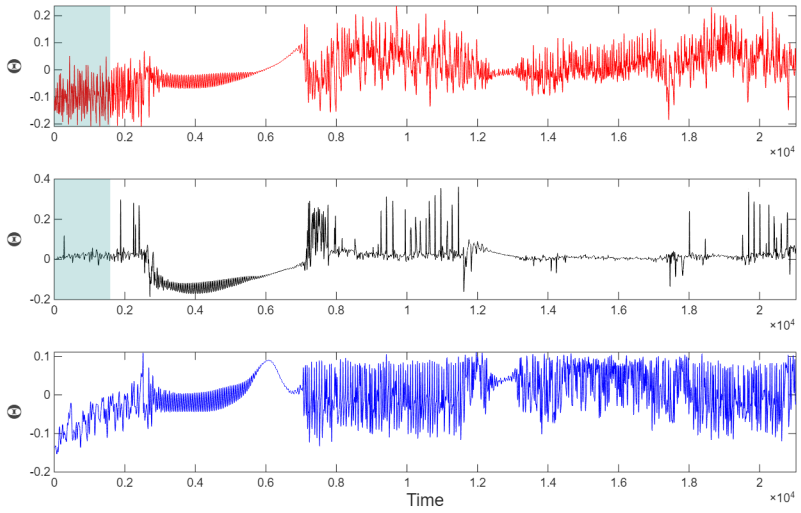


Figure 8. Temperature fluctuations at three representative locations in the computational domain for $Ra = 2.5 \times 10^5$. The red curve corresponds to the point $(x, z) = (1.3374, 0.9741)$, located near the upper boundary; the black curve corresponds to $(x, z) = (1.7278, 0.4772)$, located in the central region of the domain; and the blue curve corresponds to $(x, z) = (1.052, 0.0259)$, located near the lower boundary.

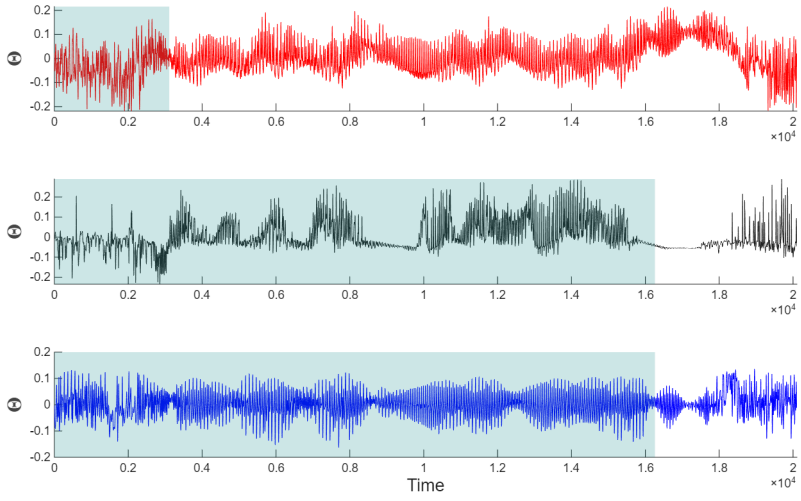


Figure 9. Temperature fluctuations at three representative locations in the computational domain for $Ra = 4 \times 10^5$. The red curve corresponds to the point $(x, z) = (2.7413, 0.9741)$, located near the upper boundary; the black curve corresponds to $(x, z) = (2.3668, 0.4772)$, located in the central region of the domain; and the blue curve corresponds to $(x, z) = (2.8996, 0.0259)$, located near the lower boundary.

5.3. *Statistical characterization*

To further characterize the intermittent dynamics, the statistical properties of the temperature fluctuations were investigated for representative values of the Rayleigh number. Particular attention was paid to the extent to which the fluctuations could be described by Gaussian probability distributions. The analysis was performed for $Ra = 2.5 \times 10^5$ and $Ra = 4.0 \times 10^5$ using three complementary diagnostics: histograms, normal Q–Q plots, and Kolmogorov–Smirnov normality tests [32].

Figures 10–15 illustrate representative examples. In several locations and over time intervals corresponding to persistent turbulent activity, the fluctuations exhibit probability distributions that are well-approximated by a Gaussian law. This behavior is reflected in the near-linear alignment of the Q–Q plots and in the relatively large p-values obtained from the Kolmogorov–Smirnov tests. For example, the fluctuations at $(x, z) = (1.3374, 0.9741)$ for $Ra = 2.5 \times 10^5$ over the time interval $h \le t \le 1586\,h$ yield a p-value of 0.053, while those at $(x, z) = (2.7413, 0.9741)$ for $Ra = 4.0 \times 10^5$ over the time interval $h \le t \le 3111\,h$ yield a p-value of 0.107. In both cases, the histogram and Q–Q plots are consistent with an approximately Gaussian distribution.

In contrast, when longer integration intervals including both turbulent and quasi-laminar phases are considered, significant deviations from Gaussianity emerge. This effect can be observed in Figures 12 and 14, where the corresponding Kolmogorov–Smirnov tests produce p-values of order 10^{-3}. The associated histograms display clear departures from a single Gaussian profile, and the Q–Q plots exhibit pronounced deviations from linearity. Similar behavior is observed at locations situated near the centers of the convection cells, where the dynamics remain weakly fluctuating and retain a strong imprint of the quasi-laminar flow structure. These observations provide statistical evidence of temporal intermittency. During intervals dominated by a single turbulent state, the fluctuations are approximately Gaussian. However, when the dataset includes transitions between turbulent and quasi-laminar configurations, the resulting distributions become distinctly non-Gaussian. Consequently, the loss of normality appears to be directly related to the coexistence of competing dynamical states.

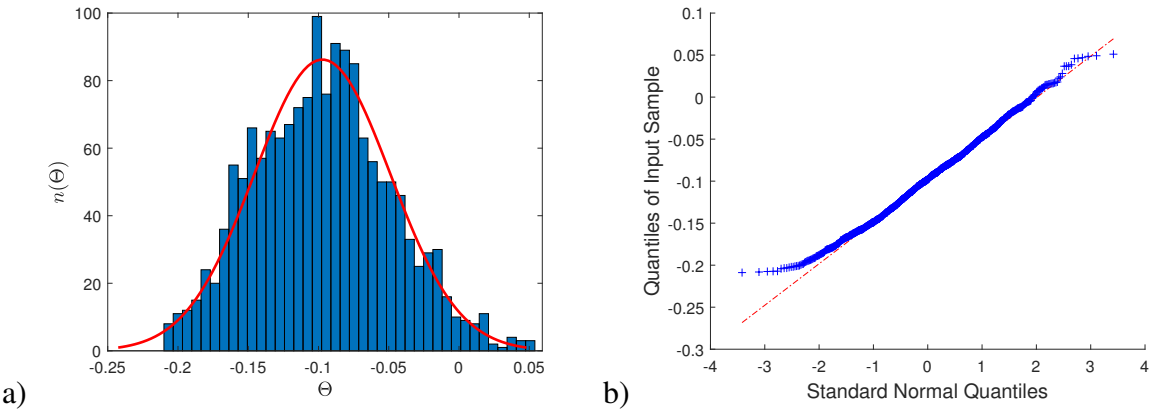
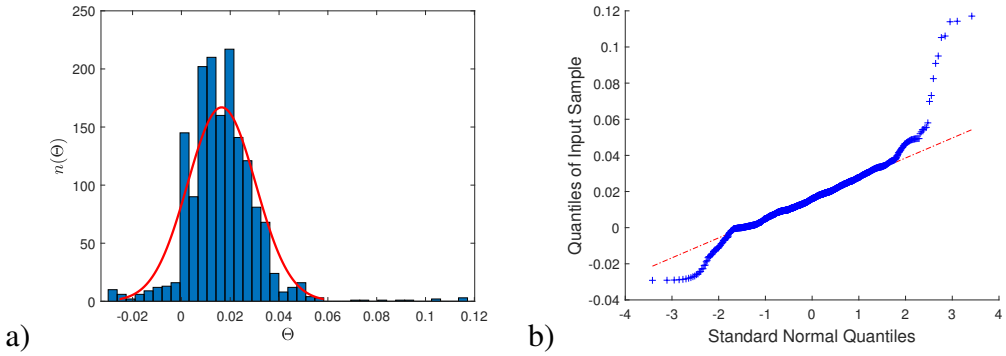
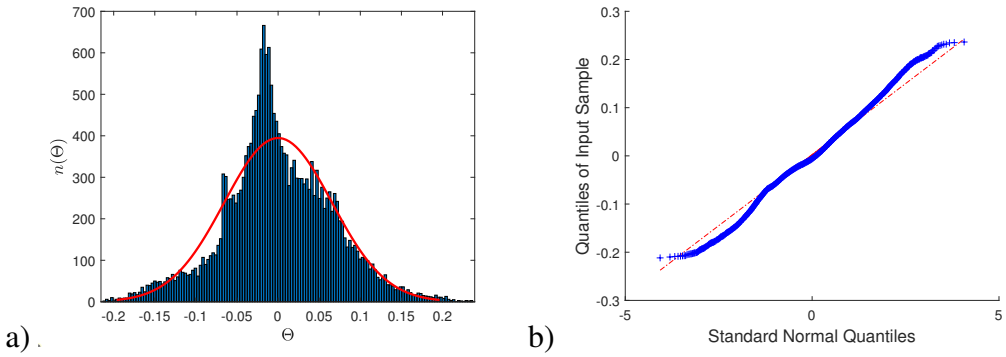


Figure 10. a) Histogram of the temperature fluctuation at $(x, z) = (1.3374, 0.9741)$ over the time interval $0 \le t \le 1586\,h$, b) Q–Q plot of the same data.



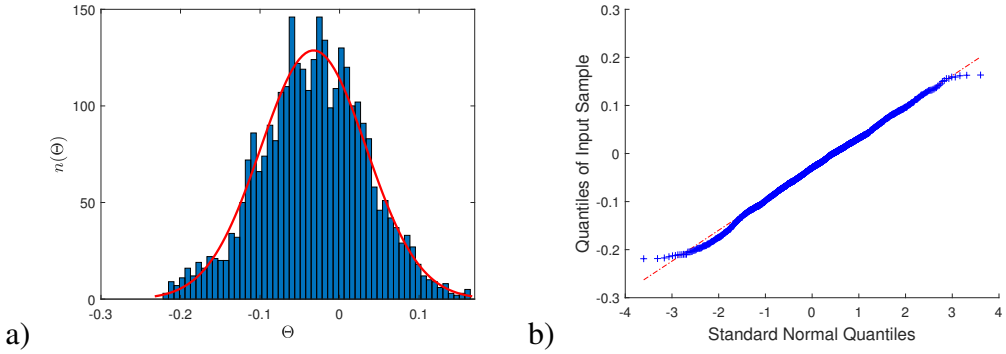
a) b)

Figure 11. a) Histogram of the temperature fluctuation at $(x, z) = (1.7278, 0.4772)$ over the time interval $0 \leq t \leq 1586\,h$, b) Q–Q plot of the same data. $Ra = 2.5 \times 10^5$.



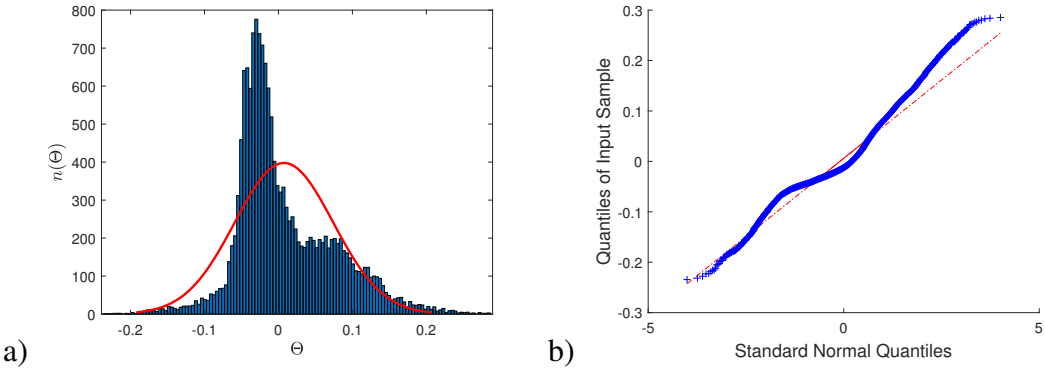
a) b)

Figure 12. a) Histogram of the temperature fluctuation at $(x, z) = (1.3374, 0.9741)$ over the time interval $0 \leq t \leq 21033\,h$, b) Q–Q plot of the same data. $Ra = 2.5 \times 10^5$.



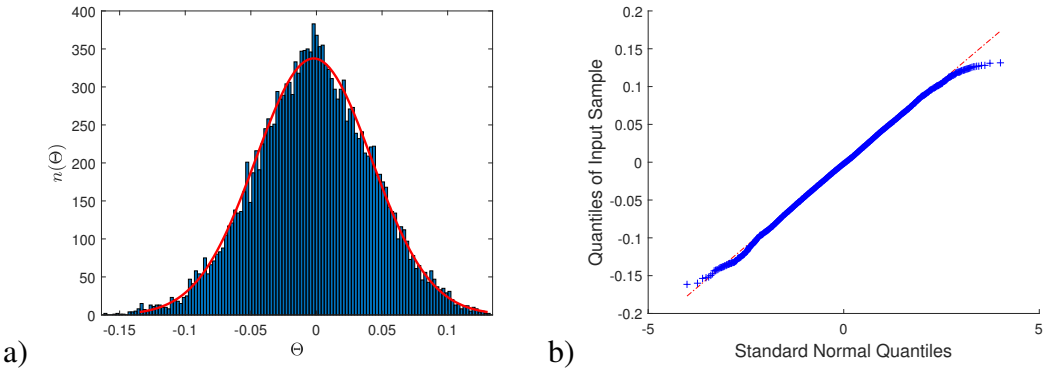
a) b)

Figure 13. a) Histogram of the temperature fluctuation at $(x, z) = (2.7413, 0.9741)$ over the time interval $0 \leq t \leq 3111\,h$, b) Q–Q plot of the same data. $Ra = 4.0 \times 10^5$.



a) b)

Figure 14. a) Histogram of the temperature fluctuation at $(x, z) = (2.3668, 0.4772)$ over the time interval $0 \leq t \leq 16260\,h$, b) Q–Q plot of the same data. $Ra = 4.0 \times 10^5$.



a) b)

Figure 15. a) Histogram of the temperature fluctuation at $(x, z) = (2.8996, 0.0259)$ over the time interval $0 \leq t \leq 16260\,h$, b) Q–Q plot of the same data. $Ra = 4.0 \times 10^5$.

To further investigate this issue, a Gaussian mixture analysis was performed for the fluctuations at $(x, z) = (1.3374, 0.9741)$ and $Ra = 2.5 \times 10^5$ over the interval $8 \times 10^3 h \leq t \leq 2.1 \times 10^4 h$. This interval contains both turbulent episodes and quasi-laminar phases and is therefore representative of the intermittent regime. The optimal number of Gaussian components was determined using the Bayesian information criterion (BIC). As shown in Figure 16, the minimum BIC value is attained for a three-component Gaussian mixture. The corresponding fit is shown in Figure 17. The three-component model reproduces the empirical distribution substantially better than a single Gaussian distribution and provides a quantitative description of the multi-stable character of the dynamics. Two of the Gaussian components are associated with the dominant flow states identified previously, whereas the third component appears to represent intermediate configurations occurring during transitions between them. The resulting decomposition therefore supports the interpretation of the flow as an intermittent dynamical system characterized by the coexistence of multiple competing attractors. In general, the statistical analysis reveals that the temperature fluctuations cannot be described by a unique universal distribution. Instead, the probability density strongly depends on the underlying dynamical regime. Gaussian statistics emerge locally within individual turbulent states, whereas Gaussian-mixture models provide a more appropriate description when transitions between distinct flow configurations are

included. These findings are consistent with previous studies of multi-stability and intermittency in turbulent thermal convection [11, 25, 57].

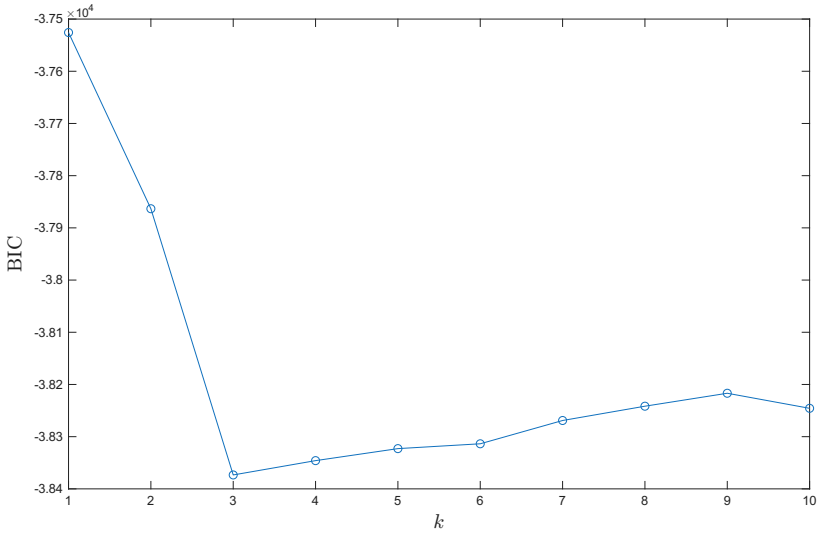
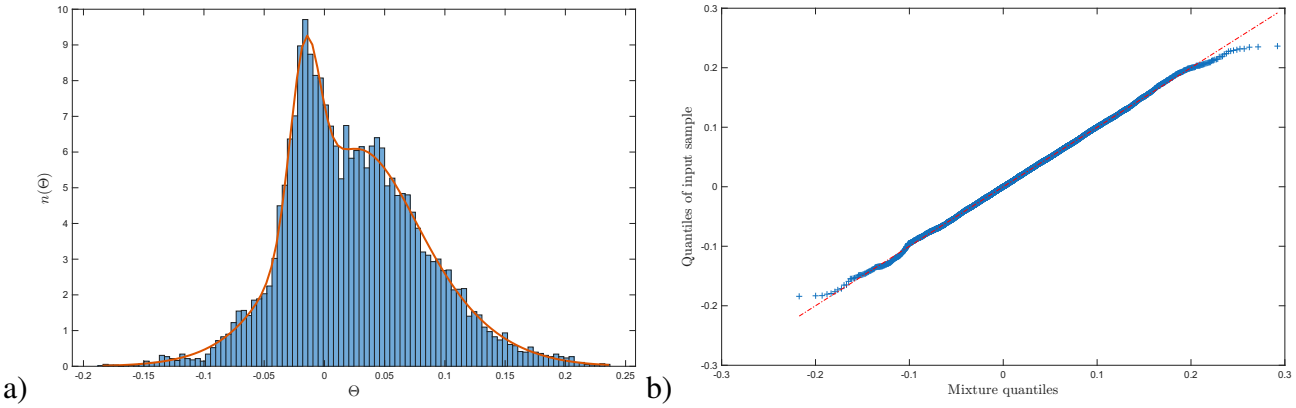


Figure 16. BIC depending on the number of clusters k for the data of the temperature fluctuation at $(x, z) = (1.3374, 0.9741)$ over the time interval $8000\,h \leq t \leq 21033\,h$ at $Ra = 2.5 \times 10^5$.



a) b)

Figure 17. a) Histogram for data of the temperature fluctuation at $(x, z) = (1.3374, 0.9741)$ over the time interval $8000\,h \leq t \leq 21033\,h$ at $Ra = 2.5 \times 10^5$ and the best fit of a 3-Gaussian mixture, b) Q–Q plot of the same data.

5.4. Heat-transfer properties and scaling laws

The implications of the intermittent dynamics for heat transport are examined through the Nusselt number defined by Eqs (4.3)–(4.4). The time series of $Nu(t)$ displayed in Figure 18 provide clear evidence of the coexistence of the two competing flow regimes identified in the previous sections. In all cases, the Nusselt number alternates between two well-defined levels, corresponding to the quasi-laminar and plume-dominated states, reflecting the intermittent switching of the flow between

distinct dynamical configurations. A remarkable feature observed in Figure 18 is that the quasi-laminar four-roll state consistently exhibits larger Nusselt numbers than the plume-dominated turbulent state. Consequently, the more organized four-roll circulation transports heat more efficiently despite being associated with weaker fluctuations. This result indicates that a higher degree of flow complexity does not necessarily lead to enhanced heat-transfer rates.

The dependence of the time-averaged Nusselt number on the Rayleigh number is summarized in Figure 19. As illustrated in Figure 19a), the steady three-roll solution branch originating at $Ra_c = 1100$ undergoes a loss of stability through a subcritical bifurcation at approximately $Ra = 2.5 \times 10^5$. This critical Rayleigh number is consistent with the value reported in Ref [10]. Beyond this threshold, the heat-transfer mechanism undergoes a qualitative transition, giving rise to an intermittent regime characterized by the coexistence of distinct flow states. A particularly significant feature of the bifurcation diagrams in Figure 19 is the presence of several hysteresis loops. Both the global diagram shown in Figure 19a) and the magnified view in Figure 19b) reveal clear discrepancies between forward and backward continuation paths. The coexistence of different branches over the same interval of Rayleigh numbers provides strong evidence of multistability and confirms that several stable or metastable states are simultaneously accessible to the flow. These observations are consistent with the intermittent alternation between the turbulent and quasi-laminar regimes identified in the Nusselt time series of Figure 18.

To characterize the heat-transfer properties of each branch, power-law regressions of the form

$$Nu = a\,Ra^b$$

were computed separately for the two flow regimes identified in Figures 18 and 19. The resulting scaling laws are as follows:

$$Nu = 0.1653\,Ra^{0.32}, \qquad Nu = 0.1543\,Ra^{0.31}.$$

Although these branches correspond to different flow organizations, the scaling exponents remain very close. Furthermore, both values are consistent with the classical scaling law

$$Nu \sim Ra^{1/3},$$

widely reported for Rayleigh–Bénard convection [2, 6, 15, 20, 40, 53]. The similarity of the exponents suggests that the two regimes differ primarily in the efficiency of heat transport, represented by the prefactor, rather than in their asymptotic scaling behavior. Overall, Figures 18 and 19 demonstrate that the transition to turbulence is governed by intermittent dynamics involving the coexistence of competing flow states. This coexistence manifests itself through multiple heat-transfer levels, hysteresis loops, and distinct Nusselt branches, while preserving the classical Nusselt–Rayleigh scaling at the global level.

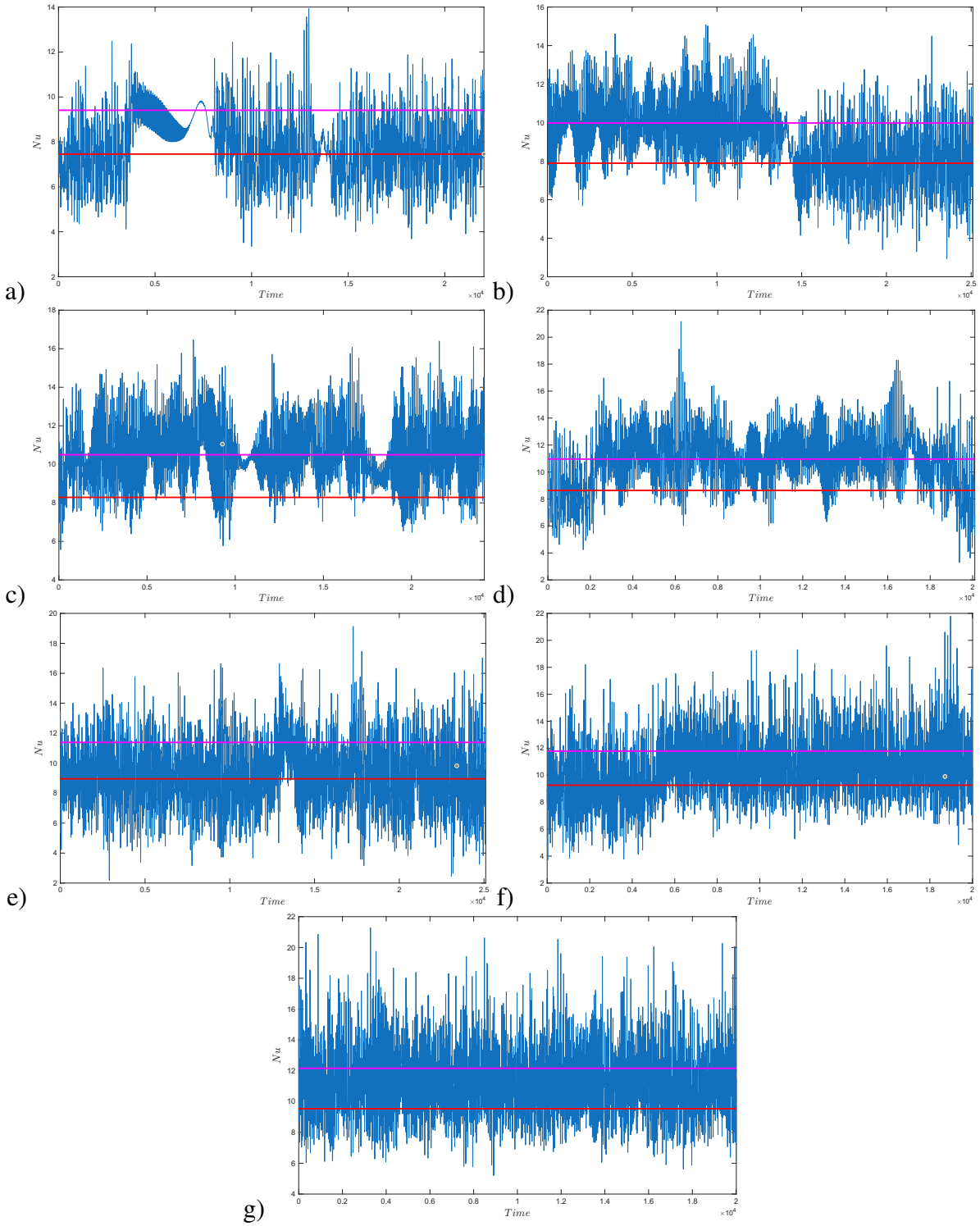


Figure 18. Time series of the Nusselt number $Nu(t)$ for increasing values of the Rayleigh number. The horizontal lines represent the mean heat-transfer rates associated with the quasi-laminar four-roll regime and the plume-dominated turbulent regime. The alternation between both levels reflects the intermittent character of the solutions and the coexistence of competing dynamical states. a) $Ra = 2.5 \times 10^5$; b) $Ra = 3.0 \times 10^5$; c) $Ra = 3.5 \times 10^5$; d) $Ra = 4.0 \times 10^5$; e) $Ra = 4.5 \times 10^5$; f) $Ra = 5.0 \times 10^5$; g) $Ra = 5.5 \times 10^5$.

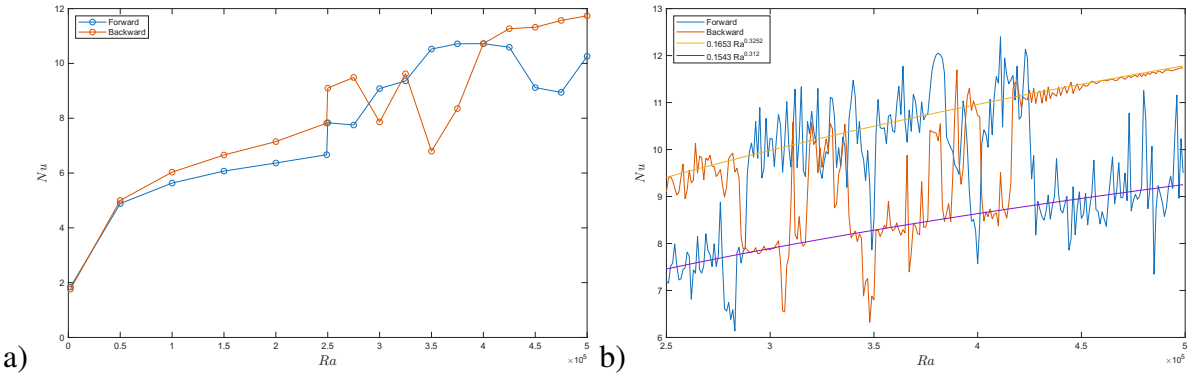


Figure 19. Bifurcation diagrams of the time-averaged Nusselt number $Nu(Ra)$ defined by Eq (4.4). Blue curves correspond to forward continuation (increasing Ra), whereas red curves correspond to backward continuation (decreasing Ra). a) Global bifurcation diagram in the interval $0 \leq Ra \leq 5 \times 10^5$ using continuation steps of 0.5×10^5. b) Enlarged view of the interval $2.5 \times 10^5 \leq Ra \leq 5 \times 10^5$ obtained with continuation steps of 10^3. The divergence between forward and backward branches reveals the presence of hysteresis and multistability, associated with the coexistence of quasi-laminar and turbulent flow regimes.

6. Conclusions

A numerical investigation of two-dimensional Rayleigh–Bénard convection with an infinite Prandtl number has been carried out using a computational framework combining a second-order finite-difference time discretization, Legendre collocation methods, and an overlapping Schwarz domain-decomposition strategy. The proposed methodology proved capable of resolving both steady and highly unsteady convective regimes over a broad range of Rayleigh numbers.

The simulations reveal the existence of a subcritical transition near $Ra \approx 2.5 \times 10^5$, where the classical steady three-roll solution loses stability and gives rise to an intermittent convective regime. Rather than evolving toward a fully developed turbulent state, the flow alternates between two competing configurations: a quasi-laminar four-roll state and a plume-dominated three-roll state characterized by enhanced small-scale activity. This coexistence persists over a wide interval of Rayleigh numbers and constitutes the dominant dynamical feature of the system.

The intermittent character of the solutions is supported by several complementary analyses. Space–time representations of temperature fluctuations show alternating intervals associated with the two flow organizations, while pointwise fluctuation signals reveal strong temporal variability. Moreover, the largest fluctuations are consistently observed near the thermal boundary layers, indicating that turbulent activity is primarily concentrated close to the upper and lower walls, where plume generation and ejection processes occur.

The statistical analysis provides additional evidence of intermittency and multistability. Gaussian statistics are recovered only over restricted temporal windows, whereas longer datasets that include both quasi-laminar and turbulent episodes exhibit clear departures from normality. Gaussian-mixture models provide a significantly improved description of the fluctuation data and support the interpretation of the dynamics as the interaction of multiple coexisting states and transitional events.

The heat-transfer properties of the flow were analyzed by the Nusselt number. The bifurcation

diagrams reveal several hysteresis loops and distinct forward and backward continuation branches, demonstrating the coexistence of multiple stable or metastable solutions for the same Rayleigh number. Interestingly, the quasi-laminar four-roll state systematically produces larger Nusselt numbers than the turbulent three-roll state, indicating that the coherent four-roll circulation transports heat more efficiently than the plume-dominated regime.

Finally, the computed heat-transfer rates obey power-law relationships of the form $Nu = aRa^b$, with exponents close to the classical value $b = 1/3$ reported in theoretical, numerical, and experimental studies of Rayleigh–Bénard convection. The computed critical thresholds, the hysteresis structure, and the Nusselt-number scalings are consistent with previous results available in the literature, thus supporting the validity of the proposed numerical methodology and the physical interpretation of the observed intermittent dynamics.

Overall, the results suggest that the transition to turbulence in the present configuration is governed by a complex multistable scenario involving the coexistence of competing flow states, hysteresis, intermittent dynamics, and multiple heat-transfer branches, while preserving the classical Nusselt–Rayleigh scaling at the global level.

Author contributions

The authors contributed equally to the conception, development, and preparation of this manuscript.

Use of Generative-AI tools declaration

The authors used Microsoft Copilot exclusively for English language correction. The tool was not used for the generation of scientific content, data analysis, mathematical derivations, numerical simulations, figures, or conclusions. The authors assume full responsibility for all content in the manuscript.

Acknowledgments

This work was partially supported by the Research Grants PID2023-152004NB-I00 (Spanish Government) and 2025-GRIN-38610 (Universidad de Castilla-La Mancha), which include Regional Development European Funds (RDEF).

Conflict of interest

The authors declare no conflict of interest.

References

1. G. Ahlers, E. Bodenschatz, D. Funfschilling, J. Hogg, Turbulent Rayleigh-Bénard convection for a Prandtl number of 0.67, *J. Fluid. Mech.* **641** (2009), 157–167. https://doi.org/10.1017/S0022112009991959

2. F. Alcántara-Ávila, S. Hoyas, Direct numerical simulation of thermal channel flow for medium-high Prandtl numbers up to Re= 2000, *Int. J. Heat and Mass Transfer*, **176** (2021), 121412. https://doi.org/10.1016/j.ijheatmasstransfer.2021.121412
3. A. Baïri a, E. Zarco-Pernia, J. M. García de María, A review on natural convection in enclosures for engineering applications, The particular case of the parallelogrammic diode cavity, *Appl. Therm. Eng.*, **63** (2014), 304–322. https://doi.org/10.1016/j.applthermaleng.2013.10.065
4. H. Bénard, Les tourbillons cellulaires dans une nappe liquide, *Rev. Gen. Sci. Pures Appl.*, **11** (1900), 1261–1271.
5. C. Bernardi, Y. Maday, Approximations spectrales des problemes aux limites elliptiques, Berlin: Springer-Verlag, 1992.
6. S. Bhattacharya, M. K. Verma, R. Samtaney, Revisiting Reynolds and Nusselt numbers in turbulent thermal convection, *Phys. Fluids*, **33** (2021), 015113. https://doi.org/10.1063/5.0032498
7. G. Boffetta, R. Ecke, Two-Dimensional Turbulence, *Annu. Rev. Fluid Mech.*, **44** (2012), 427–451. https://doi.org/10.1146/annurev-fluid-120710-101240
8. J. Boussinesq, Theorie analytique de la chaleur, Vol. 2, Gauthier-Villars, 1903.
9. C. Canuto, M. Hussaini, A. Quarteroni, T. Zang, Spectral methods in fluid dynamics, Berlin: Springer-Verlag, 1988. https://doi.org/10.1007/978-3-642-84108-8
10. X. Chavanne, F. Chilla, B. Chabaud, B. Castaing, B. Hebral, Turbulent Rayleigh-Bénard convection in gaseous and liquid He, *Phys. Fluids*, **13** (2001), 1300–1320. https://doi.org/10.1063/1.1355683
11. E. S. C. Ching, C. K. Leung, X. L. Qiu, P. Tong, Intermittency of velocity fluctuations in turbulent thermal convection, *Phys. Rev. E*, **68** (2003), 026307. https://doi.org/10.1103/PhysRevE.68.026307
12. G. Chini, Exact coherent structures at extreme Reynolds number, *J. Fluid Mech.*, **791** (2016), 97–121. https://doi.org/10.1017/jfm.2016.154
13. M. Caponeri, S. Ciliberto, Thermodynamics aspects of the transition to spatiotemporal chaos, *Physica D*, **58** (1992), 365–383.
14. S. Ciliberto, Several aspects of the transition to spatiotemporal chaos, *Ann. Phys.*, **19** (1994), 715–720.
15. P. Constantin, C. Doering, Infinite Prandlt number convection, *J. Stat. Phys.*, **94** (1999), 159–172. https://doi.org/10.1023/A:1004511312885
16. G. F. Davies, Dynamic Earth– Plates, Plumes and Mantle Convection, Cambridge: Cambridge University Press, 2000. https://doi.org/10.1017/CBO9780511605802
17. M. Dubois, Experimental aspects of the transition to turbulence in Rayleigh–Bénard convection, *Lecture Notes Phys.*, **164** (2005), 177–191. https://doi.org/10.1007/3-540-11581-1_6
18. P. F. Fisher, An overlaping Schwarz method for spectral element solution of the incompressible Navier-Stokes equations, *J. Comput. Phys.*, **133** (1997), 84–101. https://doi.org/10.1006/jcph.1997.5651
19. S. R. Ghias, G. T. Jarvis, Mantle convetion models with temperature and depth-dependent thermal expansivity, *J. Geophys. Res. Solid Earth*, **113** (2008), 1–15. https://doi.org/10.1029/2007JB005355

20. S. Grossmann, D. Lohse, Thermal convection for large Prandtl numbers, *Phys. Rev. Lett.*, **86** (2001), 3316. https://doi.org/10.1103/PhysRevLett.86.3316
21. H. Herrero, A. M. Mancho, On presssure boundary conditions for thermoconvective problems, *Int. J. Numer. Meth. Fluids*, **39** (2002), 391–402. https://doi.org/10.1002/fld.317
22. H. Herrero, S. Hoyas, A. Donoso, A. M. Mancho, J. M. Chacón, R. F. Portugués, et al., Chebyshev collocation for a convective problem in primitive variable formulation, *J. Sci. Comput.*, **8** (2003), 312–328. https://doi.org/10.1023/A:1022678124929
23. H. Herrero, F. Pla, M. Ruiz-Ferrández, A Schwarz Method for a Rayleigh-Bénard Problem, *J. Sci. Comput.,* **78** (2018), 376–392. https://doi.org/10.1007/s10915-018-0771-1
24. H. Herrero, Y. Maday, F. Pla. RB (Reduced basis) for RB (Rayleigh-Bénard), *Comput. Methods Appl. Mech. Engrg.*, **261-262** (2013), 132–141. https://doi.org/10.1016/j.cma.2013.02.018
25. X. He, Y. Wang, P. Tong, Dynamic heterogeneity and conditional statistics of non-Gaussian temperature fluctuations in turbulent thermal convection, *Phys. Rev. Fluids*, **3** (2018), 052401(R). https://doi.org/10.1103/PhysRevFluids.3.052401
26. B. Holmedal, Stability of squares and rolls in Rayleigh-Bénard convection in an infinite-Prantl-number fluid between slabs, *J. Fluid Mech.,* **537** (2005), 271–284. https://doi.org/10.1017/S0022112005005240
27. S. D. King, C. Lee, P. E. van Keken, W. Leng, S. J. Zhong, E. Tan, et al., A community benchmark for 2-D Cartesian compressible convection in the Earth's mantle, *Geophysical J. Int.*, (2010), 73–87. https://doi.org/10.1111/j.1365-246X.2009.04413.x
28. G. L. Kooij, M. A. Botchev, E. M. A. Frederix, B. J. Geurts, S. Horn, D. Lohse, et al., Comparison of computational codes for direct numerical simulations of turbulent Rayleigh-Bénard convection, *Comput. Fluids*, **166** (2018), 1–8. https://doi.org/10.1016/j.compfluid.2018.01.010
29. P. Kooloth, D. Sondak, L. M. Smith, Coherent solutions and transition to turbulence in two-dimensional Rayleigh-Bénard convection, *Phys. Rev. Fluids*, **6** (2021), 013501. https://doi.org/10.1103/PhysRevFluids.6.013501
30. D. Krug, X. Zhu, D. Chung, I. Marusic, R. Verzicco, D. Lohse, Transition to ultimate Rayleigh-Bénard turbulence revealed through extended self-similarity scaling analysis of the temperature structure functions, *J. Fluid Mech.*, (2018), 024502. https://doi.org/10.1017/jfm.2018.561
31. M. Lappa, Thermal convection: patterns, evolution and stability, New York: John Wiley & Sons, 2009.
32. H. W. Lilliefros, On the Kolmogorov-Smirnov Test for Normality with Mean and Variance, *J. Am. Stat. Assoc.*, **62** (1967), 399–402.
33. A. V. Malevsky, Patterns of convective turbulence- an effect of Prandtl number, *Phys. Earth Planet. In.*, **88** (1995), 31–41. https://doi.org/10.1016/0031-9201(94)05074-8
34. P. Manneville, Rayleigh-Bénard convection: Thirty years of experimental, theoretical, and modeling work, *Centenary Review*, **207** (2006), 41–65. https://doi.org/10.1007/978-0-387-25111-0_3
35. D. Martínez, H. Herrero, F. Pla, 2D Newton Schwarz Legendre collocation method for a convection problem, *Mathematics*, **10** (2022), 3718. https://doi.org/10.3390/math10193718

36. D. Martínez, F. Pla, H. Herrero, A. Fernández-Pérez, A Schwarz alternating method for an evolution convection problem, *Appl. Num. Math.*, **192** (2023), 179–196.https://doi.org/10.1016/j.apnum.2023.06.007
37. D. Martínez, H. Herrero, F. Pla, Implicit Schwarz domain decomposition method for a Rayleigh-Bénard problem, *J. Comput. Appl. Math.,* **470** (2025), 116718. https://doi.org/10.1016/j.cam.2025.116718
38. L. N. Moresi, V. S. Solomatov, Numerical investigation of 2D convection with extremely large viscosity variations, *Phys. Fluids*, **7** (1995), 2154–2162. https://doi.org/10.1063/1.868465
39. M. C. Navarro, D. Castaño, H. Herrero, Thermoconvective instabilities to explain the main characteristics of a dust devil-like vortex, *Physica D*, **308** (2015), 109–115. https://doi.org/10.1016/j.physd.2015.06.010
40. J. Niemela, L. Skrbek, K. Sreenivasan, R. Donnelly, Turbulent convection at very high Rayleigh numbers, *Nature*, **404** (2000), 837–840. https://doi.org/10.1038/35009036
41. A. Nikolaenko, G. Ahlers, Nusselt number measurements for turbulent Rayleigh-Bénard convection, *Phys. Rev. Lett.*, **91** (2003), 084501. https://doi.org/10.1103/PhysRevLett.91.084501
42. F. Otto, C. Seis, Rayleigh-Bénard convection: Improved bounds on the Nusselt number, *J. Math. Phys.*, **52** (2011), 083702. https://doi.org/10.1063/1.3623417
43. A. Pandey, M. K. Verma, A. G. Chatterjee, B. Dutta, Similarities between 2D and 3D convection for large Prandtl number, *Pramana-J. Phys.*, **87** (2016), 1–10. https://doi.org/10.1007/s12043-016-1204-z
44. F. Pla, A. M. Mancho, H. Herrero, Bifurcation phenomena in a convection problem with temperature dependent viscosity at low aspect ratio, *Physica D*, **238** (2009), 572–280. https://doi.org/10.1016/j.physd.2008.12.015
45. E. P. van der Poel, R. J. A. M. Stevens, D. Lohse, Comparison between two- and three-dimensional Rayleigh-Bénard convection, *J. Fluid Mech.*, **736** (2013), 177–194. https://doi.org/10.1017/jfm.2013.488
46. J. D. M. Rademacher, R. Welter, Energetic consistency and heat transport in Fourier-Galerkin truncations of free slip 3D rotating convection, *Nonlinearity*, **39** (2025), 075010. https://doi.org/10.48550/arXiv.2505.07678
47. P. Ho-Liu, B. H. Hager, A. Raefsky, An improved method of Nusselt number calculation, *Geophys. J. Int.*, **88** (1987), 205–215. https://doi.org/10.1111/j.1365-246X.1987.tb01375.x
48. K. R. Rajagopal, M. Ruzicka, A. R. Srinivasa, On the Oberbeck-Boussinesq approximation, *Math. Mod. Meth. Appl. Sci.,* **6** (1996), 1157–1167. https://doi.org/10.1142/S0218202596000481
49. J. D. Scheel, M. S. Emran, J. Schumaker, Resolving the fine-scale structure in turbulent Rayleigh-Bénard convection, *New J. Phys.*, **15** (2013), 113063. https://doi.org/10.1088/1367-2630/15/11/113063
50. J. Schmalzl, M. Breuer, U. Hansen, On the validity of two-dimensional numerical approaches to time-dependent thermal convection, *Europhys. Lett.*, **67** (2004), 390–396. https://doi.org/10.1209/epl/i2003-10298-4
51. G. Schubert, D. L. Turcotte, P. Olson, Mantle Convection in the Earth and Planets, Cambridge: Cambridge University Press, 2009.

52. O. Shishkina, S. Horn, S. Wagner, E. S. C. Ching, Thermal boundary layer equation for turbulent Rayleigh-Bénard convection, *Phys. Rev. Lett.*, **114** (2015), 114302. https://doi.org/10.1103/PhysRevLett.114.114302
53. E. D. Siggia, High Rayleigh number convection, *Annu. Rev. Fluid Mech.*, **26** (1994), 137–168. https://doi.org/10.1146/annurev.fl.26.010194.001033
54. J. C. Strikwerda, Finite Difference Schemes for Partial Differential Equations, Philadelphia: SIAM, 1989.
55. D. L. Turcotte, *Convection*, *Reviews of Geophysics*, **17** (1979), 1090–1098.
56. R. Verzicco, P. Orlandi, A finite-difference scheme for three-dimensional incompressible flow in cylindrical coordinates, *J. Comput. Phys.,* **123** (1996), 402–414. https://doi.org/10.1006/jcph.1996.0033
57. Y. Wang, X. Z. He, P. E. Tong, Turbulent temperature fluctuations in a closed Rayleigh-Bénard convection cell, *J. Fluid Mech.*, **874** (2019), 263–284. https://doi.org/10.1017/jfm.2019.405
58. H. G. Weller, G. Tabor, H. Jasak, C. Fureby, A tensorial approach to computational continuum mechanics using object.oriented techniques, *Comput. Phys.*, **12** (1998), 620–631. https://doi.org/10.1063/1.168744
59. Y. C. Xie, G. Y. Ding, K. Q. Xia, Flow Topology Transition via Global Bifurcation in Thermally Driven Turbulence, *Phys. Rev. Lett.*, **120** (2018), 214501. https://doi.org/10.1103/PhysRevLett.120.214501
60. V. Yakhot, 4/5 Kolmogorov law for statistically stationary turbulence- Application to high Rayleigh number Bénard convection, *Phys. Rev. Lett.*, **69** (1992), 769–771. https://doi.org/10.1103/PhysRevLett.69.769
61. T. Yanagita, K. Kaneko, Rayleigh-Bénard convection-patterns, chaos, spatiotemporal chaos and turbulence, *Physica D*, **82** (1995), 288–313. https://doi.org/10.1016/0167-2789(94)00233-G
62. S. Zaleski, P. Lallemand, Scaling laws and intermittency in phase turbulence, *J. Physique Lett.*, **46** (1985), 793–797. https://doi.org/10.1051/jphyslet:019850046017079300
63. Q. Zhou, C. Sun, K. Q. Xia, Experimental investigation of homogeneity, isotropy, and circulation of the velocity field in buoyancy-driven turbulence, *J. Fluid Mech.*, **598** (2008), 361–372. https://doi.org/10.1017/S0022112008000189



AIMS Press

© 2026 the Author(s), licensee AIMS Press. This is an open access article distributed under the terms of the Creative Commons Attribution License (http://creativecommons.org/licenses/by/4.0)